

ARTICLE

Received 22 Feb 2015 | Accepted 30 Jul 2015 | Published 11 Sep 2015

DOI: 10.1038/ncomms9239

OPEN

Strong correlations elucidate the electronic structure and phase diagram of $\text{LaAlO}_3/\text{SrTiO}_3$ interface

E. Maniv¹, M. Ben Shalom¹, A. Ron¹, M. Mograbi¹, A. Palevski¹, M. Goldstein¹ & Y. Dagan¹

The interface between the two band insulators SrTiO_3 and LaAlO_3 has the unexpected properties of a two-dimensional electron gas. It is even superconducting with a transition temperature, T_c , that can be tuned using gate bias V_g , which controls the number of electrons added or removed from the interface. The gate bias-temperature (V_g , T) phase diagram is characterized by a dome-shaped region where superconductivity occurs, that is, T_c has a non-monotonic dependence on V_g , similar to many unconventional superconductors. Here, we report, the frequency of the quantum resistance-oscillations versus inverse magnetic field for various V_g . This frequency follows the same non-monotonic behaviour as T_c ; a similar trend is seen in the low field limit of the Hall coefficient. We theoretically show that electronic correlations result in a non-monotonic population of the mobile band, which can account for the experimental behaviour of the normal transport properties and the superconducting dome.

¹Raymond and Beverly Sackler School of Physics and Astronomy, Tel-Aviv University, Levanon Street, Tel Aviv 69978, Israel. Correspondence and requests for materials should be addressed to Y.D. (email: yodagan@post.tau.ac.il).

When LaAlO₃ is epitaxially grown on TiO₂-terminated {100} SrTiO₃, conductivity appears starting from a LaAlO₃ thickness threshold of four unit cells^{1,2}. The transport properties as well as the superconducting ones are strongly dependent on gate bias^{2–5}. Recently, conducting interface has also been observed in {110} SrTiO₃/LaAlO₃ interfaces⁶. Gate bias can be either applied by biasing the back of the substrate relative to the conducting layer (back gate) or by applying the electric field across the thin dielectric LaAlO₃ layer (top gate)⁷. Superconductivity at the interface is observed over a carrier density range of a few 10¹³ cm⁻² but is suppressed at higher densities. In bulk SrTiO₃, superconductivity is known to depend on the number of charge carriers^{8,9} and it appears in one or two bands depending on carrier density¹⁰. In contrast with SrTiO₃/LaAlO₃, in bulk SrTiO₃, superconductivity extends over a broad region of charge densities. It has been proposed that two-dimensional fluctuations destroy superconductivity in the low carrier regime³. However, it is still difficult to understand why superconductivity disappears at a relatively low density on the overdoped side of the phase diagram of SrTiO₃/LaAlO₃.

Previously, we have found evidence for the existence of multiple bands in SrTiO₃/LaAlO₃ (ref. 11). Santander-Syro *et al.*¹² showed that in conducting SrTiO₃ surface, the degeneracy of the titanium (Ti) *t*_{2g} bands is removed by the surface and they split into a lower-energy *d*_{xy} band, and *d*_{yz} and *d*_{xz} bands that are filled at higher gate biases. Joshua *et al.*¹³ introduced an atomic spin-orbit coupling term that mixes the three bands into a new, more complex, band structure. Nernst effect and magnetotransport measurements¹⁴ suggested that the mobile band is the one responsible for superconductivity. Another view is by Joshua *et al.*¹³, who suggested that a second band becomes populated exactly at a critical density where the superconducting critical temperature *T*_c is maximal. This issue is still a matter of debate.

In this study we use the Shubnikov-de Haas (SdH) effect (probing the area of the Fermi surface), as well as the resistivity and the low field limit of the inverse Hall coefficient *R*_H⁻¹ (which is dominated by the density of the mobile charge carriers), to study the band structure of the SrTiO₃/LaAlO₃ interface. We show that the SdH frequency and *R*_H⁻¹ follow a non-monotonic behaviour similar to the dependence of the superconducting critical temperature *T*_c and magnetic field *H*_c on gate bias. Both the SdH frequency and *R*_H⁻¹ exhibit an anomalous decrease on increasing the gate bias beyond maximum *T*_c. We interpret this unconventional decrease as arising from electronic correlations between the Ti *t*_{2g} bands that are mixed by the atomic spin-orbit interaction. Our calculations show that in this case the population of the mobile band and its density of states (DOS) are non-monotonic functions of the chemical potential (*μ*). This can explain the peculiar gate dependence of the transport properties, as well as the decrease in *T*_c on the overdoped regime in the (*V*_g, *T*) phase diagram.

Results

Experimental data. We use three samples of {100} LaAlO₃/SrTiO₃ interface patterned into Hall bars (see Methods for full description). Sample A was used to study the superconducting dome and the low-field Hall effect, and Samples B and C were used for studying the low-field Hall effect and the gate dependence of the SdH frequency.

Figure 1 presents the sheet resistance of Sample A, normalized by its value at *T* = 800 mK for the same gate bias. Defining *T*_c as the temperature for which *R*(*T*_c) = *R*(*T* = 800 mK)/2, the green contour represents *T*_c as a function of *V*_g. *T*_c is maximal for *V*_g = 2.6 ± 0.3 V. The entire superconducting dome is revealed by varying *V*_g by

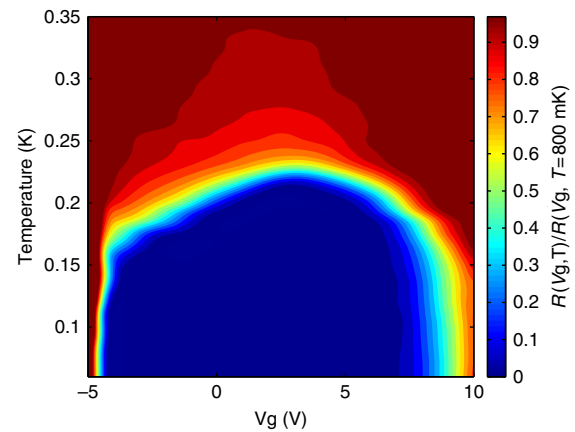


Figure 1 | Superconducting phase diagram. A colour map of the normalized resistance plotted as a function of gate bias and temperature. Each resistance value is divided by the resistance at *T* = 800 mK (above *T*_c) and the same value of *V*_g (Sample A).

merely 15 V, thus demonstrating the performance of our gate design¹⁵.

The shape of the superconducting dome is somewhat different from the previously reported one³. In particular, in the vicinity of the base of the dome the gate dependence of *T*_c is very sharp. At both edges of the superconducting dome, the equiresistance lines are almost perpendicular to the gate bias axes. For *V*_g ≤ -4.8 V, this behaviour persists into the normal state and hence may not reflect intrinsic properties of the material, but may arise from the contacts becoming non-ohmic. This region is not relevant for our experiment. The fine-tunability of our devices allows us to study in detail the dependence of the magneto-transport properties and the superconductivity on gate bias.

Figure 2a presents the longitudinal resistivity as a function of magnetic field for several fixed gate biases for Sample A. Superconductivity is suppressed at fields greater than the critical magnetic field, *H*_c, defined as *R*(*H*_c) = *R*(*T* = 800 mK)/2.

In the lower inset of Fig. 2b, we show the sheet resistance of Sample B versus high magnetic field for *V*_g = 3 V. SdH oscillations can be seen. In order to make them clearer, we subtracted a monotonic polynomial background from the data and used a low-pass filter to remove noise (Fig. 2b). Additional data for Sample B is presented in Supplementary Figs 1b and 4a, and for Sample C in Supplementary Figs 2 and 4b. The upper inset shows a fast Fourier transform (FFT) used to find the SdH frequency for the data in the lower inset. We found the frequency to be independent of the analysis and background subtraction as explained in the Methods section.

We note that Sample B had both back and top gate electrodes. The latter was prepared using an additional e-beam lithography process, which apparently ruined the superconducting transition. However, all other properties of this sample remained similar to those of samples A, C and other samples previously measured.

We shall now examine carefully the gate dependence of the superconducting and transport properties, to demonstrate that the low field limit of the Hall coefficient, the frequency of the SdH effect, *T*_c and *H*_c all exhibit similar non-monotonic behaviour as a function of gate bias. In Fig. 3a, the inverse low-field Hall coefficient (*eR*_H)⁻¹ in units of carrier density is plotted as a function of *V*_g measured at 60 mK for Sample A. Below 1 K (*eR*_H)⁻¹ is practically temperature independent. Yellow squares are data taken with a fixed *V*_g while scanning the field from -3 *T* to +3 *T* and fitting a linear curve up to 3 *T* to the antisymmetric part. The low-field data is completed by the magenta circles,

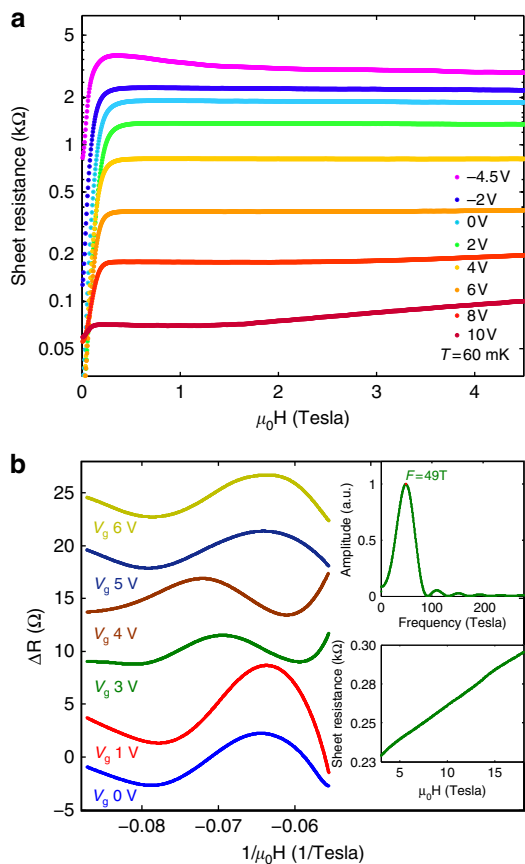


Figure 2 | Low and high field measurements. (a) Sheet resistance is plotted on a logarithmic scale as a function of magnetic field at $T = 60$ mK for various fixed values of gate bias V_g (Sample A). (b) Resistance versus inverse magnetic field after subtraction of a smooth polynomial background for various fixed values of gate bias V_g (Sample B). Successive curves are shifted by 5Ω for clarity. Lower inset: the resistance per square at $V_g = 3$ V versus the magnetic field. Upper inset: FFT of the $V_g = 3$ V data.

which represent the Hall number inferred from the transverse voltage measured for $\mu_0 H = \pm 3$ T after antisymmetrizing the data. The data taken using these two methods coincide, indicating that the Hall signal is approximately linear in field up to 3 T, as can be seen in Fig. 3a. A clear non-monotonic signal is observed with a maximum at $V_g = 2.45 \pm 0.3$ V. We also plot H_c (blue diamonds), defined by $R(H_c) = R(T = 800$ mK)/2. H_c , T_c and $(eR_H)^{-1}$ are all non-monotonic. The maximum of $(eR_H)^{-1}$ and that of T_c and H_c appear at the same gate bias within error: $V_g = 2.6 \pm 0.2$ V.

The non-monotonic behaviour of $(eR_H)^{-1}$ appears to be a universal property of the $\text{LaAlO}_3/\text{SrTiO}_3$ interface, independent of LaAlO_3 layer thickness (between 6 and 16 unit cells). It can also be seen in other reports with various film thickness: for example, ref. 4 (10 unit cells), ref. 13 (6 and 10 unit cells) and ref. 16 (10 unit cells). In Fig. 3a, it is presented for 6 unit cells with a much higher resolution. This behaviour is reproduced for 16 unit cells in Fig. 3b and for a third sample of 16 unit cells in Supplementary Fig. 3.

To better understand which bands govern the low-field Hall coefficient $(eR_H)^{-1}$, we studied it together with the SdH frequency, which is a direct clean measurement of the number of carriers in the mobile band. The SdH signal of less mobile bands is strongly suppressed by its exponential dependence on the Dingle scattering time. We plot $(eR_H)^{-1}$ and the SdH frequency for Sample B as function of back gate bias in Fig. 3b.

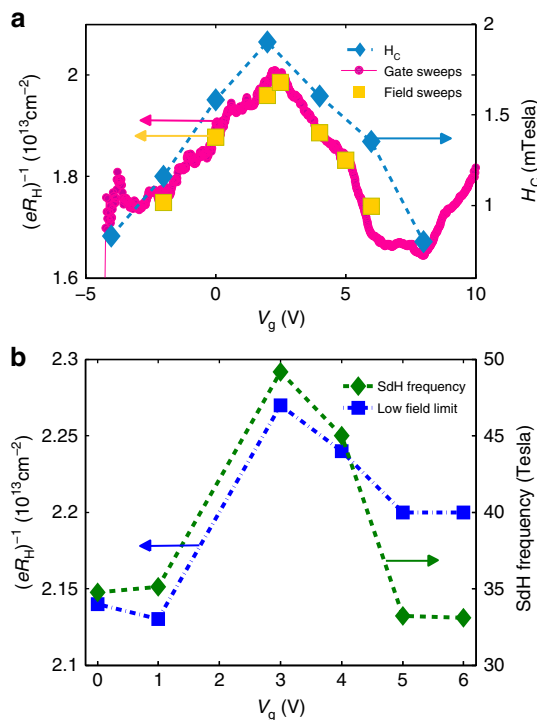


Figure 3 | Non-monotonic behaviour of the transport and superconducting properties.

(a) (Sample A) left axis (indicated by yellow and magenta arrows): the inverse of the Hall coefficient is plotted as a function of the gate bias for a fixed magnetic field of 3 T (magenta circles). The Hall coefficient was also extracted by measuring the Hall resistance as a function of the magnetic field from 0 to 3 T and using a linear fit (yellow squares). Right axis (indicated by a blue arrow): superconducting critical magnetic field H_c , defined as $R(T = 60$ mK, $H_c) = 1/2R(T = 800$ mK, $H = 0)$, plotted for different fixed gates bias values at $T = 60$ mK (blue diamonds). (b) (Sample B) left axis (indicated by a blue arrow): the inverse of the Hall coefficient inferred from a linear fit to the data in Supplementary Fig. 1c up to 2 T is plotted as a function of the gate bias (blue squares). Right axis (indicated by a green arrow): the SdH frequency is plotted as a function of the gate bias (green diamonds). The SdH frequency is calculated from FFT analysis of the data in Fig. 2b.

Blue squares are the Hall coefficients $(eR_H)^{-1}$ at low magnetic fields extracted from a linear fit to the Hall resistance data in Supplementary Fig. 1c between 0 and 2 T. Green diamonds are the SdH frequency, calculated from FFT of the data in Fig. 2b. Both quantities follow the same non-monotonic behaviour despite an order-of-magnitude difference in the carrier densities they correspond to, as previously noted by Ben Shalom *et al.*¹¹. This means that the population of the mobile band decreases with increasing total number of carriers (increasing gate bias). The nonlinear response of SrTiO_3 to electric field¹⁷ cannot account for the non-monotonic effects that we observe, as the dielectric function is monotonic as function of the electric field, and, moreover, the total carrier density should in any case increase monotonically with the applied gate voltage. Therefore, such a scenario is possible only if electronic interactions are considered, as we now discuss. Sample C showed the same behaviour of decreasing SdH and $(eR_H)^{-1}$ for increasing gate bias (see Supplementary Fig. 3).

Theoretical analysis and results. To interpret our results we employ a minimal theoretical model of three t_{2g} bands (d_{xy} , d_{xz} and d_{yz}), split and mixed by atomic spin-orbit coupling,

as suggested by Joshua *et al.*¹³. The main new ingredient in our model is a Hubbard-type repulsion between electrons occupying different orbitals in the same unit cell. We use a mean-field approximation in which an electron in a certain orbital $i = xy, xz, yz$ experiences an average increase of $U_{ij}N_j$ in its energy, owing to repulsion by electrons in orbital j , with N_j being the average occupancy of electrons in the j^{th} orbital per unit cell (summed over spin). The intra-band interaction between electrons of opposite spins is $\frac{1}{2}U_{ii}N_i$. The orbital populations are calculated self-consistently, as explained in the theoretical methods section. For simplicity, we took the interaction energy $U_{ij} = U = 2.7 \text{ eV}$ both for the intra- and inter-band interactions for all orbitals, consistent with ref. 18.

Owing to the interactions, on increasing the chemical potential μ (that is, increasing the gate bias) the band structure is modified, as demonstrated in Fig. 4a–c, where the band structure is presented for different values of μ . Each of the three bands should be slightly split, owing to the Rashba spin–orbit coupling. We neglect this effect, as it is very small, as demonstrated in Supplementary Fig. 6 (although it is important for the parallel-field dependence of superconductivity⁵ and for the weak anti-localization effect¹⁹).

In addition, scanning superconducting quantum interference device (SQUID) measurements detected free magnetic moments at the interface²⁰ and magnetization measurement^{21,22} found evidence for a magnetic phase at elevated temperatures. However, the latter measurements were performed at significant magnetic fields, presumably sufficient to align the moments. We have recently found evidence for a magnetic order at zero field below 1 K (ref. 23). The energy scale of this interaction is very low compared with the terms in the presented Hamiltonian.

Therefore, and in order to keep our calculations simple, we did not allow for a Stoner instability.

The resulting total densities of electrons in each band are presented in Fig. 4d. Although the electron density in the lowest-energy band 1 (red line in Fig. 4a–c) is monotonically increasing with μ , the electron density in band 2, which is populated next (blue line in Fig. 4a–c) has a non-monotonic dependence on μ (it is noteworthy that the overall electron density is still monotonic with μ). In Fig. 4e, we present the calculated single-particle DOS for band 2, which exhibits a similar non-monotonic μ -dependence.

To calculate the Hall resistance we employ a model of point impurities. In the absence of orbital mixing, this would lead to momentum-independent scattering rates for each band. In that case, in the two-band regime, the low-field limit of the inverse Hall coefficient $(eR_H)^{-1}$ would be $(eR_H)^{-1} = \frac{(n_1\zeta_1 + n_2\zeta_2)^2}{n_1\zeta_1^2 + n_2\zeta_2^2}$, with ζ_i being the mobility and n_i the carrier density of the unmixed i^{th} band (orbital). With band mixing the situation is more complicated, as the composition of the bands in terms of the original t_{2g} orbitals changes as function of the momentum and as function of μ . We performed the corresponding calculations, taking the carrier densities from Fig. 4d, and assigning mobilities of 6,000 and 500 $\text{cm}^2\text{V}^{-1}\text{s}^{-1}$ to the unmixed d_{xy} and d_{yz}/d_{xz} bands, respectively, roughly representing the ratio of the unmixed bands' effective masses. The resulting low-field inverse Hall coefficient $(eR_H)^{-1}$ is shown in Fig. 4e. The calculated $(eR_H)^{-1}$ is non-monotonic as function of the chemical potential and its maximum appears at the same μ as the maximum of the DOS of band 2 (blue). This behaviour is similar to the observed dependence of the measured $(eR_H)^{-1}$ as function of gate bias for all samples.

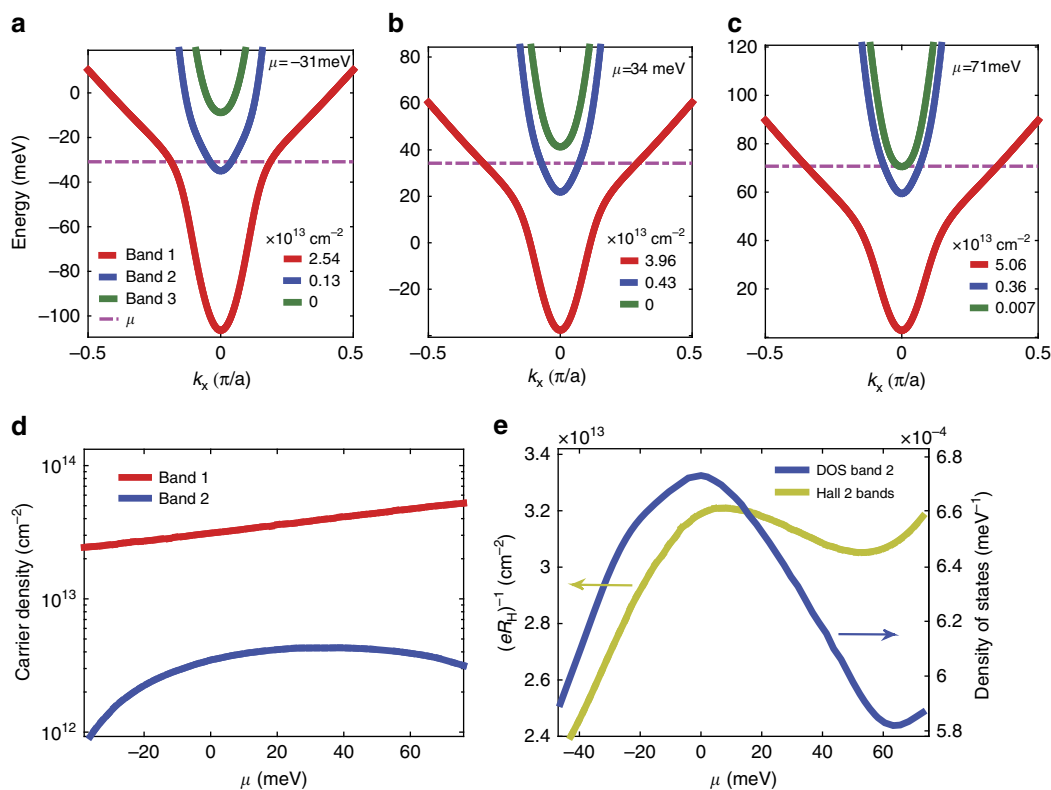


Figure 4 | Results of the theoretical model. (a–c) Band structure including the effects of mean-field electronic correlations for three different chemical potentials μ . A cut through the centre of the Brillouin zone along the k_x axis is shown. The calculated carrier densities for each band are shown. (d) The carrier concentration of the two lower bands (band 1 and band 2). A non-monotonic behaviour of the carrier density of band 2 is obtained. (e) Left axis (indicated by a yellow arrow): calculated inverse Hall coefficient in the low field limit as a function of μ . Right axis (indicated by a blue arrow): the DOS per unit cell of band 2. Both properties show non-monotonic behaviour with a maximum at a similar value of μ .

Discussion

In a simple capacitor, one expects the carrier concentration to monotonically increase with gate voltage (even in the presence of nonlinear dielectric materials such as SrTiO₃). By contrast, in our experiment we see a non-monotonic behaviour of the SdH frequency and $(eR_H)^{-1}$ as a function of gate bias. Our theoretical model does give rise to such non-monotonic behaviour as seen in Fig. 4. What is the reason for this theoretical result? Electronic interactions cause a competition between the occupancies of different bands: when the population of one band increases, the energies of the states in the other band are shifted and the other band's occupation decreases. In the presence of such a competition, occupying the band with the highest single-particle DOS is usually preferable, as this results in lower single-particle energy. As Fig. 4a–c reveals, at low energies band 1 is mainly composed of low effective mass (low DOS) d_{xy} orbitals, but at higher energies it gains a heavier (high DOS) d_{xz}/d_{yz} character; the opposite occurs for the band 2. Thus, as the gate bias, and hence μ , are increased from large negative values, the following occurs: (i) initially band 1 is occupied, because its energy is lower. As it becomes progressively filled, the energy of band 2 increases (Fig. 4a); (ii) at some point, μ reaches the bottom of the shifted band 2, where band 2's DOS is large, and it begins to fill up (Fig. 4b); (iii) at higher μ , when band 1 becomes heavier than band 2, it becomes preferable to increase the population of band 1 further at the expense of band 2 (Fig. 4c). The population of band 2 is thus non-monotonic as a function of μ . A similar population switching effect has recently been discussed in the context of quantum dot physics, where a narrow (high DOS) level may increase in occupancy at the expense of a broad (low DOS) one (see, for example, refs 24–29).

In Fig. 5a we compare the calculated carrier density of band 2 (blue) and the one extracted from the frequency F of the SdH signal for Sample B through $n = eF/\pi\hbar$. First, we note that the calculation gives the right order of magnitude for the carrier density. Second, the non-monotonic behaviour of the SdH frequency is reproduced by the calculation. The chemical potential was shifted and scaled such that the maximum in the calculated carrier density and the maximal measured SdH frequency coincide. This scaling is consistent with the estimated capacitance of our devices¹⁵. Furthermore, as both bands contribute to the Hall coefficient, while only the mobile second band (whose population is suppressed by the interaction effects) contributes to the SdH, our model naturally explains the order-of-magnitude difference between $(eR_H)^{-1}$ and the density corresponding to the SdH frequency, which has hitherto been a puzzle¹¹.

Our analysis implies that band 1 has much lower mobility than band 2. This could be due to the fact that in the gate voltage region corresponding to the non-monotonic behaviours, band 1 is mainly composed of the heavier d_{xz} – d_{yz} orbitals, whereas band 2 mainly includes the lighter d_{xy} orbital. It should be noted that at lower values of μ (before band 2 enters), band 1 has a d_{xy} character but is still not observed in SdH. This can be accounted for using the density functional theory calculations of Delugas *et al.*³⁰. They find that at low values of μ the d_{xy} orbital resides in Ti atoms at the STO/LAO interface, where scattering centres are expected to reside, whereas at higher values of μ the d_{xy} orbital moves to Ti atoms away from the interface. This picture is also in line with the transport measurements of Bell *et al.*⁴ and with the observed difference between the effects of top and bottom gates on the transport properties⁷. These two gate configurations can effect the location of the wave function along the z -direction in an opposite way.

As the theoretically calculated DOS ρ_2 of the band 2 (blue) has a similar non-monotonic behaviour as the measured $(eR_H)^{-1}$

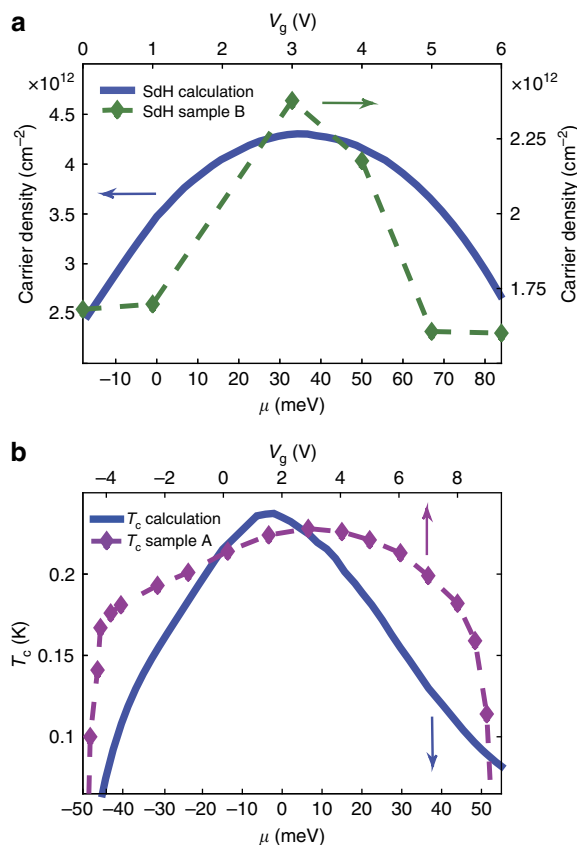


Figure 5 | Comparing experimental data and theoretical calculations.

(a) Bottom left axes (indicated by a blue arrow): the carrier density of band 2 (taken from Fig. 4d) is plotted as a function of μ . Top right axes (indicated by a green arrow): the carrier density inferred from the SdH frequency in Fig. 3b is plotted as a function of the gate bias V_g . Both show a similar behaviour as function of V_g or μ (which are related through the gate capacitance). (b) Top axis (indicated by a purple arrow): critical temperature of Sample A (taken from Fig. 1) is plotted as a function of V_g . Bottom axis (indicated by a blue arrow): critical temperature calculated from the weak-coupling BCS formula using the DOS of band 2 (taken from Fig. 4e) is plotted as a function of chemical potential μ . Both critical temperatures exhibit a non-monotonic behaviour with a maximum at the same μ (V_g) as the inverse Hall coefficient.

and T_c , it is tempting to try and compare the measured T_c with the weak-coupling single-band BCS formula, $T_c \approx 1.13T_D e^{-1/\rho_2 V_{BCS}}$. To obtain the correct order of magnitude for T_c with the measured Debye temperature $T_D = 400$ K of SrTiO₃ (ref. 31), we use electron–phonon coupling energy $V_{BCS} = 0.196$ eV. This value is within the weak coupling limit for all the calculated DOS values used.

In Fig. 5b, we plot the calculated T_c together with the measured one (taken from Fig. 1) with μ and V_g scaled to match the superconducting dome region. The non-monotonic behaviour of T_c is reproduced. Using the same scaling, the calculated and measured $(eR_H)^{-1}$ showed the same behaviour as a function of μ and V_g (see Supplementary Fig. 5). Although using a single-band BCS model is probably an oversimplification (and indeed for the low carrier densities a non-BCS type behaviour has been reported in planar tunnelling measurements³²), it is interesting to see that it can nicely capture the behaviour of T_c versus gate bias in a SrTiO₃/LaAlO₃ interface and, in particular account for the decrease in T_c on the overdoped regime.

In summary, we found that the SdH frequency, the inverse low-field Hall coefficient and the superconducting transition temperature all exhibit a similar non-monotonic dependence on gate bias. To explain our data we employed a model involving electronic correlation between the spin-orbit split titanium t_{2g} bands. In this model, the second band, which is populated in a non-monotonic manner at higher gate bias values, is the one responsible for the SdH effect and for superconductivity.

Methods

Experimental. We grow epitaxial layers of LaAlO₃ using reflection high-energy electron diffraction-monitored pulsed laser deposition on atomically flat TiO₂-terminated {100} SrTiO₃ 0.5-mm thick substrates in standard conditions, oxygen partial pressure of 1×10^{-4} Torr and temperature of 780 °C, as described in ref. 33. In the first step, two unit cells of LaAlO₃ are deposited. Next, Hall bars of $9 \times 3 \mu\text{m}^2$ (A) $12 \times 3 \mu\text{m}^2$ (B) and $20 \times 5 \mu\text{m}^2$ (C) are patterned using electron beam (A) or optical (B and C) lithography followed by deposition of a 40-nm-thick amorphous BaTiO₃ layer and lift-off to define the conducting channel, where an additional layer of LaAlO₃ is epitaxially grown in the final step. The total LaAlO₃ thickness is 6 (16) unit cells for Sample A (B and C). The design aims to minimize screening from the contact pads and leads, thus enhancing the gate bias effectivity. The strong response to back-gating is possible for dielectric substrates with high permittivity (high ϵ) when the distance d between the gate electrode and the tunable surface (or interface) becomes much larger than the width of the mesoscopic conducting channel ℓ . This results in a capacitance per area of the order of 5×10^{12} (electrons $\times \text{cm}^{-2} \text{V}^{-1}$) for $d = 0.5 \text{ mm}$, $\ell = 3 \mu\text{m}$, an order of magnitude larger than for standard planar capacitor geometry¹⁵.

Gold gate electrodes are evaporated to cover the back of the substrate. The leakage current is unmeasurably small ($< 1 \text{ pA}$). The resistivity and low field measurements of Sample A were performed in a dilution refrigerator with a base temperature of 60 mK using a Princeton Applied Research 124-A lock-in amplifier. During cool down, the gate bias was scanned back and forth while recording the temperature and measuring the sheet (per square) resistance. The gate scan is reversible within a 2-mV resolution, as long as the maximal gate bias (10 V) is not exceeded. The high field measurements were performed on Sample B and C. Sample B was measured in a dilution refrigerator with a base temperature of 20 mK at magnetic fields of up to 18 T and a constant top gate voltage of 1 V. Sample C was measured in a He3 cryostat with a base temperature of 350 mK and at magnetic fields of up to 34.5 T. Both samples B and C were measured using a Lakeshore 370 resistivity bridge with 3,716 L low-resistance preamplifier and scanner at Tallahassee National High Magnetic Field Laboratory.

For the SdH analysis, we first subtracted a smooth polynomial background as described in ref. 11. We made sure that the background consists of no oscillations, and that the frequency is independent of the background chosen. The background was fitted using a polynomial with a maximum order of 4. The frequency is found both by using FFT analysis with a step-type window function and manually (using the distance between the extrema in the data). Both methods give similar results within an error margin that we estimate to be 5%–10%.

Theoretical. We describe our system using the model introduced in ref. 13, to which we add local (Hubbard) interactions in the mean-field approximation. In k -space, the Hamiltonian is a 6×6 matrix in the basis of three orbitals ($i = xy, xz, yz$) $\otimes 2$ spin states ($s = \uparrow, \downarrow$). It is a sum of three terms, $H(k) = H_0(k) + H_{\text{SO}}(k) + H_{\text{int}}(k)$, the first of which being

$$H_0(k) = \begin{pmatrix} \epsilon_{xy}(k) - \Delta_E & 0 & 0 \\ 0 & \epsilon_{xz}(k) & 2t_l \sin(k_x a) \sin(k_y a) \\ 0 & 2t_l \sin(k_x a) \sin(k_y a) & \epsilon_{yz}(k) \end{pmatrix} \otimes I_2 \quad (1)$$

with

$$\epsilon_{xy}(k) = 2t_l [2 - \cos(k_x a) - \cos(k_y a)] \quad (2)$$

$$\epsilon_{xz}(k) = 2t_l [1 - \cos(k_x a)] + 2t_l [1 - \cos(k_y a)] \quad (3)$$

$$\epsilon_{yz}(k) = 2t_l [1 - \cos(k_x a)] + 2t_l [1 - \cos(k_y a)], \quad (4)$$

where $a = 3.905 \text{ \AA}$ is the SrTiO₃ lattice constant, $t_l = 875 \text{ meV}$, $t_h = 40 \text{ meV}$ and $t_d = 40 \text{ meV}$ are, respectively, the light, heavy and yz - xz mixing tunnelling matrix elements. Through the relation $t_{l/h} = \hbar^2 / (2m_{l/h} a^2)$, these correspond to light/heavy effective masses of $m_l = 0.7 m_e$ and $m_h = 15 m_e$, respectively. $\Delta_E = 47 \text{ meV}$ is the relative shift between the xy and xz/yz orbitals due to the confinement potential at the SrTiO₃/LaAlO₃ interface. We neglect orbital coupling, owing to the asymmetric confining potential and the Rashba term (see Supplementary Fig. 6). Following XAS³⁴, ARPES¹², and transport¹³ results, we assume that the other d_{xy} sub-band predicted by density functional theory calculations³⁰ are localized and do not play a role in transport, following in this respect previous theoretical studies^{13,35}.

Atomic spin-orbit coupling contributes

$$H_{\text{SO}}(k) = \frac{i\Delta_{\text{SO}}}{2} \begin{pmatrix} 0 & \sigma_x & -\sigma_y \\ -\sigma_x & 0 & \sigma_z \\ \sigma_y & -\sigma_z & 0 \end{pmatrix}, \quad (5)$$

with $\Delta_{\text{SO}} = 40 \text{ meV}$.

Finally, the mean-field interaction term is

$$H_{\text{int}} = \begin{pmatrix} E_{\text{int}}^{xy} & 0 & 0 \\ 0 & E_{\text{int}}^{xz} & 0 \\ 0 & 0 & E_{\text{int}}^{yz} \end{pmatrix} \otimes I_2, \quad (6)$$

where $E_{\text{int}}^i = \sum_j U_{ij} (1 - \delta_{ij}/2) N_j$ ($ij = xy, xz, yz$), where N_j is the average occupancy of orbital j (summed over spin) per unit cell. The subtracted term in E_{int}^i removes the unphysical self-interaction of electrons in the same orbital and spin state. The matrix U_{ij} is symmetric. Moreover, the symmetries of our system dictate that $U_{xy, xz} = U_{xy, yz}$ and $U_{xz, xz} = U_{yz, yz}$. In our calculations, we take for simplicity all the elements to be equal, $U_{ij} = U = 2.7 \text{ eV}$. The average occupancies N_j are determined self-consistently, taking into account the contributions of the different eigenstates of the Hamiltonian weighted by their decomposition in terms of the orbitals and the Fermi-Dirac distribution, $f(\epsilon) = 1/[e^{(\epsilon - \mu)/k_B T} + 1]$: denoting the eigenvectors of the matrix $H(k)$ by $\psi_{m,\tau}(k; i, s)$, with corresponding eigenvalues $\epsilon_{m,\tau}(k)$ ($i = xy, xz, yz$ and $s = \uparrow, \downarrow$ denote the bare orbital and spin, whereas $m = 1, 2, 3$ denote the bands and $\tau = \pm 1$ is a Kramers spin index), we have

$$N_j = \sum_{m,\tau,s} \int_{\text{BZ}} \frac{a^2 d\mathbf{k}}{(2\pi)^2} |\psi_{m,\tau}(k; j, s)|^2 f[\epsilon_{m,\tau}(k)], \quad (7)$$

where the integration is over the first Brillouin zone.

After the self-consistency equations have been solved, the total density of electrons populating band $m = 1, 2, 3$ (related to the frequency of the SdH oscillations) can be calculated as:

$$n_m = \sum_{\tau} \int_{\text{BZ}} \frac{d\mathbf{k}}{(2\pi)^2} f[\epsilon_{m,\tau}(k)]. \quad (8)$$

The local DOS (per unit cell) ρ_m of band m at the Fermi energy is the derivative of $a^2 n_m$ with respect to μ , keeping the mean-field interaction-induced energy shifts E_{int}^i constant.

References

- Ohtomo, A. & Hwang, H. A high-mobility electron gas at the LaAlO₃/SrTiO₃ heterointerface. *Nature* **427**, 423–426 (2004).
- Thiel, S., Hammerl, G., Schmehl, A., Schneider, C. & Mannhart, J. Tunable quasi-two-dimensional electron gases in oxide heterostructures. *Science* **313**, 1942–1945 (2006).
- Caviglia, A. *et al.* Electric field control of the LaAlO₃/SrTiO₃ interface ground state. *Nature* **456**, 624–627 (2008).
- Bell, C. *et al.* Dominant mobility modulation by the electric field effect at the LaAlO₃/SrTiO₃ interface. *Phys. Rev. Lett.* **103**, 226802 (2009).
- Ben Shalom, M., Sachs, M., Rakhmievitch, D., Palevski, A. & Dagan, Y. Tuning spin-orbit coupling and superconductivity at the SrTiO₃/LaAlO₃ interface: A magnetotransport study. *Phys. Rev. Lett.* **104**, 126802 (2010).
- Annadi, A. *et al.* Anisotropic two-dimensional electron gas at the LaAlO₃/SrTiO₃ (110) interface. *Nat. Commun.* **4**, 1838 (2013).
- Hosoda, M., Hikita, Y., Hwang, H. Y. & Bell, C. Transistor operation and mobility enhancement in top-gated LaAlO₃/SrTiO₃ heterostructures. *Appl. Phys. Lett.* **103**, 103507 (2013).
- Schooley, J. F., Hosler, W. R. & Cohen, M. L. Superconductivity in semiconducting SrTiO₃. *Phys. Rev. Lett.* **12**, 474–475 (1964).
- Lin, X., Zhu, Z., Fauqué, B. & Behnia, K. Fermi surface of the most dilute superconductor. *Phys. Rev. X* **3**, 021002 (2013).
- Lin, X. *et al.* Critical doping for the onset of a two-band superconducting ground state in SrTiO₃/LaAlO₃. *Phys. Rev. Lett.* **112**, 207002 (2014).
- Ben Shalom, M., Ron, A., Palevski, A. & Dagan, Y. Shubnikov-de Haas oscillations in SrTiO₃/LaAlO₃ interface. *Phys. Rev. Lett.* **105**, 206401 (2010).
- Santander-Syro, A. *et al.* Two-dimensional electron gas with universal subbands at the surface of SrTiO₃. *Nature* **469**, 189–193 (2011).
- Joshua, A., Pecker, S., Ruhman, J., Altman, E. & Ilani, S. A universal critical density underlying the physics of electrons at the LaAlO₃/SrTiO₃ interface. *Nat. Commun.* **3**, 1129 (2012).
- Lerer, S., Ben Shalom, M., Deutscher, G. & Dagan, Y. Low-temperature dependence of the thermomagnetic transport properties of the SrTiO₃/LaAlO₃ interface. *Phys. Rev. B* **84**, 075423 (2011).
- Rakhmievitch, D. *et al.* Anomalous response to gate voltage application in mesoscopic LaAlO₃/SrTiO₃ devices. *Phys. Rev. B* **87**, 125409 (2013).
- Herranz, G. *et al.* Engineering two-dimensional superconductivity and Rashba spin-orbit coupling in LaAlO₃/SrTiO₃ quantum wells by selective orbital occupancy. *Nat. Commun.* **6**, 6028 (2015).
- Christen, H.-M., Mannhart, J., Williams, E. J. & Gerber, C. Dielectric properties of sputtered SrTiO₃ films. *Phys. Rev. B* **49**, 12095–12104 (1994).

18. Breitschaft, M. *et al.* Two-dimensional electron liquid state at LaAlO₃/SrTiO₃ interfaces. *Phys. Rev. B* **81**, 153414 (2010).
19. Caviglia, A. *et al.* Tunable rashba spin-orbit interaction at oxide interfaces. *Phys. Rev. Lett.* **104**, 126803 (2010).
20. Bert, J. A. *et al.* Direct imaging of the coexistence of ferromagnetism and superconductivity at the LaAlO₃/SrTiO₃ interface. *Nat. Phys.* **7**, 767–771 (2011).
21. Li, L., Richter, C., Mannhart, J. & Ashoori, R. Coexistence of magnetic order and two-dimensional superconductivity at LaAlO₃/SrTiO₃ interfaces. *Nat. Phys.* **7**, 762–766 (2011).
22. Ariando, X. *et al.* Electronic phase separation at the LaAlO₃/SrTiO₃ interface. *Nat. Commun.* **2**, 188 (2011).
23. Ron, A., Maniv, E., Graf, D., Park, J. -H. & Dagan, Y. Anomalous magnetic ground state in an LaAlO₃/SrTiO₃ interface probed by transport through nanowires. *Phys. Rev. Lett.* **113**, 216801 (2014).
24. Field, M. *et al.* Measurements of Coulomb blockade with a noninvasive voltage probe. *Phys. Rev. Lett.* **70**, 1311–1314 (1993).
25. Lindemann, S. *et al.* Bouncing states in quantum dots. *Phys. Rev. B* **66**, 161312 (2002).
26. Johnson, A. C., Marcus, C. M., Hanson, M. P. & Gossard, A. C. Coulomb-modified fano resonance in a one-lead quantum dot. *Phys. Rev. Lett.* **93**, 106803 (2004).
27. Baltin, R., Gefen, Y., Hackenbroich, G. & Weidenmüller, H. Correlations of conductance peaks and transmission phases in deformed quantum dots. *Eur. Phys. J. B* **10**, 119–129 (1999).
28. Silvestrov, P. G. & Imry, Y. Towards an explanation of the mesoscopic double-slit experiment: A new model for charging of a quantum dot. *Phys. Rev. Lett.* **85**, 2565–2568 (2000).
29. Goldstein, M., Berkovits, R., Gefen, Y. & Weidenmüller, H. A. Transmission phase of quantum dots: testing the role of population switching. *Phys. Rev. B* **79**, 125307 (2009).
30. Delugas, P. *et al.* Spontaneous 2-dimensional carrier confinement at the *n*-type SrTiO₃/LaAlO₃ interface. *Phys. Rev. Lett.* **106**, 166807 (2011).
31. Burns, G. Comment on the low temperature specific heat of ferroelectrics, antiferroelectrics, and related materials. *Solid State Commun.* **35**, 811–814 (1980).
32. Richter, C. *et al.* Interface superconductor with gap behaviour like a high-temperature superconductor. *Nature* **502**, 528–531 (2013).
33. Ben Shalom, M. *et al.* Anisotropic magnetotransport at the SrTiO₃/LaAlO₃ interface. *Phys. Rev. B* **80**, 140403 (2009).
34. Salluzzo, M. *et al.* Orbital reconstruction and the two-dimensional electron gas at the LaAlO₃/SrTiO₃ interface. *Phys. Rev. Lett.* **102**, 166804 (2009).
35. Diez, M. *et al.* Giant negative magnetoresistance driven by spin-orbit coupling at the LaAlO₃/SrTiO₃ interface. *Phys. Rev. Lett.* **115**, 016803 (2015).

Acknowledgements

We thank I. Neder for useful discussions. Special thanks to J.-H. Park, D. Graf and Glover E. Jones for help in the magnet lab. This work was supported in part by the Israeli Science Foundation under grant number 569/13 by the Ministry of Science and Technology under contract 3-11875 and by the US-Israel bi-national science foundation (BSF) under grants 2010140 and 2014202. A portion of this work was performed at the National High Magnetic Field Laboratory, which is supported by National Science Foundation Cooperative Agreement Number DMR-0654118, the State of Florida, and the U.S. Department of Energy.

Author contributions

E.M., M.B.S. and A.R. equally contributed to this work. E.M., A.R., M.B.S. and Y.D. designed the experiment. E.M., M.B.S., A.R. and M.M. performed the transport measurements and analysed the data. E.M., M.B.S. and A.R. prepared the samples. E.M., A.R. and M.G. performed theoretical calculations. All authors discussed the data and wrote the paper.

Additional information

Supplementary Information accompanies this paper at <http://www.nature.com/naturecommunications>

Competing financial interests: The authors declare no competing financial interests.

Reprints and permission information is available online at <http://npg.nature.com/reprintsandpermissions/>

How to cite this article: Maniv, E. *et al.* Strong correlations elucidate the electronic structure and phase diagram of LaAlO₃/SrTiO₃ interface. *Nat. Commun.* **6**:8239 doi: 10.1038/ncomms9239 (2015).



This work is licensed under a Creative Commons Attribution 4.0 International License. The images or other third party material in this article are included in the article's Creative Commons license, unless indicated otherwise in the credit line; if the material is not included under the Creative Commons license, users will need to obtain permission from the license holder to reproduce the material. To view a copy of this license, visit <http://creativecommons.org/licenses/by/4.0/>